Wu *et al. Satellite Navigation* (2024) 5:7
https://doi.org/10.1186/s43020-023-00126-1

Satellite Navigation
https://satellite-navigation.springeropen.com/

ORIGINAL ARTICLE Open Access

Improving the underwater navigation performance of an IMU with acoustic long baseline calibration

Paipai Wu[1], Wenfeng Nie[1*], Yangfan Liu[1,2] and Tianhe Xu[1]

Abstract

Underwater acoustic Long-Baseline System (LBL) is an important technique for submarine positioning and navigation. However, the high cost of the seafloor equipment and complex construction of a seafloor network restrict the distribution of the LBL within a small area, making an underwater vehicle difficult for long-distance and high-precision acoustic-based or inertial-based navigation. We therefore propose an acoustic LBL-based Inertial Measurement Unit (IMU) calibration algorithm. When the underwater vehicle can receive the acoustic signal from a seafloor beacon, the IMU is precisely calibrated to reduce the cumulative error of Strapdown Inertial Navigation System (SINS). In this way, the IMU is expected to maintain a certain degree of accuracy by relying solely on SINS when the vehicle reaches out the range of the LBL network and cannot receive the acoustic signal. We present the acoustic LBL-based IMU online calibration model and analyze the factors that affect the accuracy of IMU calibration. The results fulfill the expectation that the gyroscope bias and accelerometer bias are the main error sources that affect the divergence of SINS position errors, and the track line of the underwater vehicle directly affects the accuracy of the calibration results. In addition, we deduce that an optimal calibration trajectory needs to consider the effects of the three-dimensional observability and position dilution of precision. In the experiment, we compare the effects of seven calibration trajectories: straight and diamond-shaped with and without the change of depth, and three sets of curves with the change of depth: circular, S-shaped, and figure-eight. Among them, we find that the figure-eight is the optimal trajectory for acoustic LBL-based IMU online calibration. We take the maintenance period during which the accumulated SINS Three Dimensional (3D) position errors are below 1 km to evaluate the calibration performance. The filed experimental results show that for the Micro-electromechanical Systems-grade IMU sensor, the maintenance period for the IMU calibrated with the proposed algorithm can be increased by 121% and 38.9% compared to the IMU without calibration and with the laboratory default parameter calibration, indicating the effectiveness of the proposed calibration algorithm.

Keywords Acoustic LBL, Online IMU calibration, SINS, Relay reference network

Introduction

The Ocean, as an important space for the sustainable development of human beings, is the main area for resource exploration and development (Stojanovic & Farmer, 2013; Yang et al., 2020). The Ocean resource exploration and development need a large amount and accurate ocean topography information, water flow, water temperature, and other information, while the underwater vehicle is an important tool for exploring the

*Correspondence:
Wenfeng Nie
wenfengnie@sdu.edu.cn
[1] Shandong Key Laboratory of Optical Astronomy and Solar-Terrestrial Environment, Institute of Space Sciences, Shandong University, Weihai 264209, Shandong, China
[2] Research Group of Astronomy and Geomatics (gAGE), Universitat Politecnica de Catalunya (UPC), Barcelona, Spain

marine environment and resources, conducting deep-sea scientific research, and deep-sea engineering operations (Levin et al., 2019; Miller et al., 2018; Wynn et al., 2014).

High-precision underwater navigation is a prerequisite for underwater vehicles to obtain such effective information and also a key factor that determines whether the vehicle can work safely and return successfully (Es-sadaoui et al., 2018; Paull et al., 2013; Stutters et al., 2008). Due to the particularity of the working environment of underwater vehicles, Global Navigation Satellite System (GNSS) cannot be applied because the electromagnetic waves of GNSS attenuates rapidly underwater (Medwin & Clay, 1998; Paull et al., 2018). Underwater vehicles can only receive satellite signals emerging from the water, which greatly reduces the continuity, safety, and concealment of the equipment. Acoustic navigation overcomes the shortcoming of rapid attenuation of electromagnetic waves in seawater, so acoustic transmitters can be used as beacons for underwater vehicles (Leonard & Bahr, 2016; Stutters et al., 2008).

At present, Long Baseline (LBL), Short Baseline (SBL), and Ultra-Short Baseline (USBL) navigation are the most widely used in acoustic navigation (Leonard & Bahr, 2016; Milne, 1983; Vickery, 1998). Among them, the LBL system can provide the most accurate position information. It relies on acoustic ranging between the underwater vehicle and the seafloor beacon. When the underwater vehicle receives the acoustic signal from a seafloor beacon, the transmission time of the acoustic signal can be determined. By knowing the local sound velocity profile and geometric position of each seafloor beacon, the position of the underwater vehicle can be determined (Kebkal & Mashoshin, 2017; Zhang et al., 2016a). However, navigation accuracy can deteriorate due to the large incident angle of the acoustic signal, and even normal navigation may become impossible when the underwater vehicle is too far from the seafloor beacon network (Fujita et al., 2006; Zhao et al., 2018).

In addition, the Strapdown Inertial Navigation System (SINS) with autonomous navigation capability can also be used for underwater navigation (Leonard et al., 1998; Stutters et al., 2008). The SINS uses the data from accelerometers and gyroscopes to obtain attitude, velocity, and position information through an integral operation, which is an autonomous navigation system with the advantages of fast measurement updating, complete measurement information, and no external interference. However, external initialization information is required before SINS can work, and the positioning error of the INS will accumulate over time (Groves, 2015; Titterton & Weston, 2004), which cannot meet the requirements of long-term and long-range underwater navigation.

The integrated navigation system of SINS/LBL is precise and stable, with good reliability and concealment (Chen et al., 2015; Zhang et al., 2016b). However, it requires a reliable seafloor reference network. Due to the high cost of the seafloor equipment and complex construction of a seafloor network, most of the seafloor reference networks are small-scaled with a limited number of seafloor beacons, for example the Dense Ocean-floor Network System for Earthquakes and Tsunamis (DONET) in Japan (Matsumoto & Araki, 2021), which are insufficient for long-term and long-distance underwater navigation services. When the underwater vehicle cannot receive acoustic signals for a long time, the SINS/LBL integrated navigation system cannot work accurately due to error accumulation.

One potential solution for the limited seafloor beacons is using acoustic signals to calibrate the Inertial Measurement Unit (IMU) of the SINS online. By receiving high-quality acoustic signals from the seafloor reference network, the acoustic ranging signal can be used to calibrate the IMU error and reduce the cumulative error. This enables the underwater vehicle to maintain a certain level of accuracy and navigate to the next seafloor reference network relying solely on the SINS when it cannot receive the acoustic signal. In fact, the concept of a relay reference network is proposed in literatures (Yang et al., 2020, 2023), which means that several small-scaled seafloor reference networks can be deployed within a certain distance. In this way, the relay reference network can be used to reduce the high cost of seafloor beacon deployment and maintenance while ensuring reliable underwater navigation services.

According to the different calibration environments, IMU calibration can be divided into laboratory in-field calibration and out-field online calibration (Poddar et al., 2017). Laboratory offline calibration refers to the use of relevant testing equipment, such as high-precision turntables, to obtain the sampling data and then perform offline processing to complete the calibration. Outfield online calibration means that the IMU and the carrier are in a fixed connection state without relying on high-precision equipment such as a turntable, and the carrier is used to maneuver to complete the excitation of the error related to the IMU. The online calibration of IMU error is completed by using information fusion technology combined with external reference information.

Compared with the laboratory in-field calibration, the out-field online calibration has the following main advantage. Considering that the IMU error changes with the service time, the external environment, and the impact of the carrier, the error parameters and characteristics of the IMU in different states are also different. Considering that the online calibration environment is the real

application environment of the IMU, the calibration results in the real application environment have higher accuracy and reliability. The difficulty of the online calibration lies in designing different calibration paths, exciting the observability of different system errors, and on this basis, improving the convergence speed and accuracy of the IMU error (Goshen-Meskin & Bar-Itzhack, 1992).

At present, there is very few research on using acoustic signals to calibrate IMU online. However, there are some studies on the use of other sensors, for example the Global Positioning System (GPS) technique, to calibrate IMU on land or aerial vehicles (Meyer & Jacob, 1994; Crassidis, 2006; Aggarwal et al., 2008; Han et al., 2009; Poddar et al., 2017; Lee et al., 2020; Ru et al., 2022). In these works, the accurate kinematic motion determined with GPS is taken as reference to calibrate the IMU errors. Usually, the deterministic and random errors of the gyroscope and accelerometer are estimated together with the state of the vehicles through the GPS/IMU integrated model. For example, Meyer and Jacob (1994) introduced the high accuracy navigation and landing system using the integrated GPS/IMU system. The in-flight calibration of the IMU was performed with the Kalman filter technique. The results demonstrated the effectiveness of the in-flight calibration, enhancing integrity, user acceptance, and confidence for the landing system, even in critical phases of flight such as an automatic landing. Therefore, GPS has been proved to be an effective technique to calibrate the IMU error online. However, due to the complex ocean environment and large variation of sound speed, there exist differences in using acoustic signal to calibrate IMU compared to the electromagnetic wave-based sensors like GPS. In addition, in terms of maneuverability, underwater vehicles have certain limitations in roll and pitch compared to aerial vehicles. Therefore, it is necessary to conduct a detailed analysis of the different factors that affect the calibrating accuracy of IMU using acoustic signals.

In the study, we aim to improve the underwater navigation performance of the IMU by acoustic long baseline calibration. The acoustic-based online calibration filter model is proposed, and we systematically analyze the factors that affect the calibration accuracy, including different types of IMU errors, different calibration trajectories, and different precision of the IMU. The paper is organized as follows. In Sect. "Acoustic-based online calibration filter model", the acoustic LBL-based IMU calibration filter model is introduced in detail. Then, the experimental results and analysis are presented in Sect. "Experimental results and analysis". Finally, the conclusions are in Sect. "Conclusion".

Acoustic-based online calibration filter model

To address the issue of error accumulation of the SINS when an underwater vehicle operates in complex ocean environments for a long time, we propose and implement an acoustic-based online calibration filter model for IMU sensors. Figure 1 illustrates the model, which comprises three modules: IMU error model, online calibration filter model, and error feedback model. When an external acoustic measurement signal is received, the system performs a measurement update and feeds back the updated IMU error through the error feedback model, which enables acoustic signals to calibrate IMU errors online.

The observability of IMU errors

Observability analysis can determine the optimal maneuvering mode for the underwater vehicle to stimulate system errors such as bias. Meanwhile it can also analyze the observability of each error under the specific maneuvers, which provides theoretical support for constructing the IMU error model. In this paper, Singular

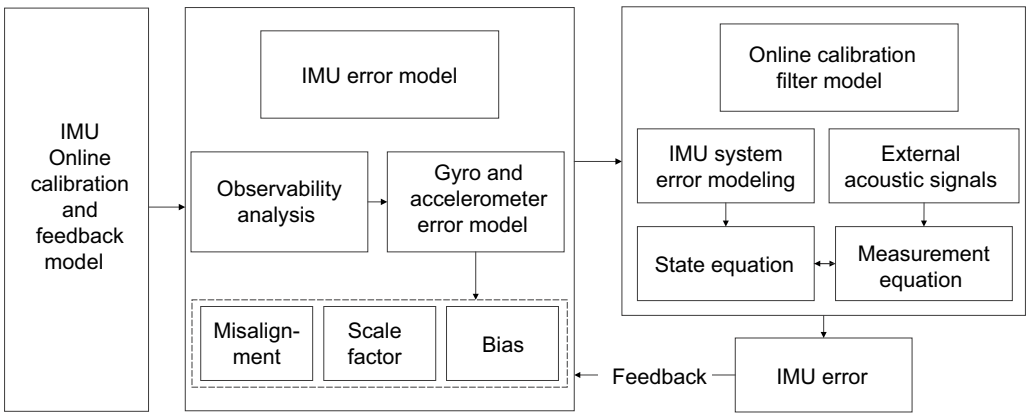

Fig. 1 The flowchart of the acoustic-based online calibration filter model

Value Decomposition (SVD) method (Goshen-Meskin & Bar-Itzhack, 1992) based on piecewise linear invariant systems is used to analyze the observability of systematic errors. The main process involves dividing the entire system into several time segments using piecewise linear invariant processing, where each segment can be considered as a linear time-invariant system. The observability matrix of the system in the ith time segment $\boldsymbol{Q}_i$ is as follows:

$$\boldsymbol{Q}_i = \left[\boldsymbol{H}_i^T \ (\boldsymbol{H}_i\boldsymbol{F}_i)^T \ \ldots \ \left(\boldsymbol{H}_i\boldsymbol{F}_i^{n-1}\right)^T \right]^T \tag{1}$$

where $\boldsymbol{F}_i$ is the constant value of the state matrix of the system in the ith time period, $\boldsymbol{H}_i$ is the observation matrix of the system, and T is the transpose of a matrix.

Combining the observability matrices at each period of the system together, the Total Observability Matrix (TOM) of the system is as follows:

$$\boldsymbol{Q}(r) = \begin{bmatrix} \boldsymbol{Q}_1 \\ \boldsymbol{Q}_2 e^{F_1\Delta_{t_1}} \\ \vdots \\ \boldsymbol{Q}_r e^{F_{r-1}\Delta_{t_{r-1}}\cdots} e^{F_1\Delta_{t_1}} \end{bmatrix} \tag{2}$$

where Δ_{t_i} is the time span of the ith period, and e means natural constant.

Introducing $\boldsymbol{Q}_s(r)$ as the extraction Observability Matrix (SOM) of the System,

$$\boldsymbol{Q}_s(r) = \left[\boldsymbol{Q}_1^T \ \boldsymbol{Q}_2^T \ \boldsymbol{Q}_3^T \ \ldots \right]^T \tag{3}$$

The SOM can be used as a substitute for the TOM to achieve observability analysis. The SVD (Goshen-Meskin & Bar-Itzhack, 1992) is applied to perform the singular value decomposition of $\boldsymbol{Q}_s(r)$:

$$\boldsymbol{Q}_s(r) = \boldsymbol{U}\boldsymbol{S}\boldsymbol{V}^T \tag{4}$$

where $\boldsymbol{S} = \begin{bmatrix} \boldsymbol{D}_n \\ \boldsymbol{0}_{(l-n)*n} \end{bmatrix}$, $\boldsymbol{D}_n$ is a diagonal matrix formed by the singular values σ_i $(i = 1, 2, \cdots, n)$ of $\boldsymbol{Q}_s(r)$, with $\sigma_1 \geq \sigma_2 \cdots \geq \sigma_m \geq 0, \sigma_{m+1} = \sigma_{m+2} = \cdots \sigma_n = 0$; $\boldsymbol{U} = \left[\boldsymbol{u}_1 \ \boldsymbol{u}_2 \ \ldots \ \boldsymbol{u}_l \right]$ and $\boldsymbol{V} = \left[\boldsymbol{v}_1 \ \boldsymbol{v}_2 \ \ldots \ \boldsymbol{v}_n \right]$ are unitary matrices of dimensions l and n, respectively. By associating the ith singular value with the state variable that corresponds to the maximum value in the ith column of matrix $\boldsymbol{V}$, the singular value of each state variable can be obtained.

The observability value of a particular state variable in the system can be determined as the ratio of its singular value σ_i to the singular value σ_0 corresponding to an external observable variable, which can be used to assess the calibration accuracy of each state variable.

The model of IMU errors

During the operation of the underwater vehicle, the measurement errors of IMU deviate significantly from their offline calibration values in the laboratory environment. To effectively calibrate and feedback IMU errors in underwater environments, this study uses an IMU error model (Stutters et al., 2008; Titterton & Weston, 2004) as follows:

$$\left.\begin{aligned} \delta\boldsymbol{\omega}_{\mathrm{ib}}^b &= \left[\delta\boldsymbol{K}_g + \delta\boldsymbol{G}\right]\boldsymbol{\omega}_{\mathrm{ib}}^b + \boldsymbol{\varepsilon}^b \\ \delta\boldsymbol{f}^b &= \left[\delta\boldsymbol{K}_a + \delta\boldsymbol{A}\right]\boldsymbol{f}^b + \boldsymbol{\nabla}^b \end{aligned}\right\} \tag{5}$$

where $\delta\boldsymbol{\omega}_{ib}^b = \left[\delta\boldsymbol{\omega}_{ibx}^b \ \delta\boldsymbol{\omega}_{iby}^b \ \delta\boldsymbol{\omega}_{ibz}^b \right]^T$ and $\delta\boldsymbol{f}^b = \left[\delta f_x^b \ \delta f_y^b \ \delta f_z^b \right]^T$ represent the measurement errors of the gyroscope and accelerometer in the body-fixed coordinate system, respectively.

$\delta\boldsymbol{G} = \begin{bmatrix} 0 & \delta G_{yz} & -\delta G_{zy} \\ -\delta G_{xz} & 0 & \delta G_{zx} \\ \delta G_{xy} & -\delta G_{yx} & 0 \end{bmatrix}$ and $\delta\boldsymbol{A} = \begin{bmatrix} 0 & \delta A_{yz} & -\delta A_{zy} \\ -\delta A_{xz} & 0 & \delta A_{zx} \\ \delta A_{xy} & -\delta A_{yx} & 0 \end{bmatrix}$ represent the misalignment matrices of the gyroscope and accelerometer, respectively. In these matrices, $\delta\boldsymbol{G}_{ij}\left(i = x, y, z;\ j = x, y, z;\ i \neq j\right)$ represents the misalignment coefficients for the three gyroscopes, and $\delta\boldsymbol{A}_{ij}\left(i = x, y, z;\ j = x, y, z;\ i \neq j\right)$ represents the misalignment coefficients for the three accelerometers. The subscripts indicate the influence of the j-axis on the i-axis. $\delta\boldsymbol{K}_g = \mathrm{diag}\left[\delta K_{gx} \ \delta\boldsymbol{K}_{gy} \ \delta\boldsymbol{K}_{gz} \right]$ and $\delta\boldsymbol{K}_a = \mathrm{diag}\left[\delta\boldsymbol{K}_{ax} \ \delta\boldsymbol{K}_{ay} \ \delta\boldsymbol{K}_{az} \right]$ represent the scale factor matrices of the gyroscope and accelerometer, respectively. $\boldsymbol{\varepsilon}^b = \left[\varepsilon_x^b \ \varepsilon_y^b \ \varepsilon_z^b \right]^T$ and $\boldsymbol{\nabla}^b = \left[\nabla_x^b \ \nabla_y^b \ \nabla_z^b \right]^T$ represent the bias matrices of the gyroscope and accelerometer, respectively. $\boldsymbol{\omega}_{ib}^b = \left[\omega_{ibx}^b \ \omega_{iby}^b \ \omega_{ibz}^b \right]^T$ and $\boldsymbol{f}^b = \left[f_x^b \ f_y^b \ f_z^b \right]^T$ represent the ideal outputs of the gyroscope and accelerometer, respectively, in the body-fixed coordinate system.

The state equation of calibration

The Kalman filtering technique is an effective method to calibrate IMU errors. In the previous section, we established the IMU error model. To enable online calibration for both the gyroscope and accelerometer, we expand the errors as state variables. As a result, a 27-dimensional online calibration filter state equation is formulated.

$$\boldsymbol{X}_{t+1} = \boldsymbol{F}_t\boldsymbol{X}_t + \boldsymbol{W}_t \tag{6}$$

In the equation, $\boldsymbol{F}_t$ is the state transition matrix,

$$\boldsymbol{F}_t = \begin{bmatrix} -(\boldsymbol{\omega}_{in}^n\times) & \boldsymbol{F}_{\phi v} & \boldsymbol{F}_{\phi p} & -\boldsymbol{C}_b^n & \boldsymbol{0}_{3\times3} & \boldsymbol{0}_{3\times3} & \boldsymbol{0}_{3\times3} & \boldsymbol{0}_{3\times3} & \boldsymbol{0}_{3\times3} \\ (\boldsymbol{C}_b^n f^b)\times & \boldsymbol{F}_{vv} & \boldsymbol{F}_{vp} & \boldsymbol{0}_{3\times3} & \boldsymbol{C}_b^n & \boldsymbol{0}_{3\times3} & \boldsymbol{0}_{3\times3} & \boldsymbol{0}_{3\times3} & \boldsymbol{0}_{3\times3} \\ \boldsymbol{0}_{3\times3} & \boldsymbol{F}_{pv} & \boldsymbol{F}_{pp} & \boldsymbol{0}_{3\times3} & \boldsymbol{0}_{3\times3} & \boldsymbol{0}_{3\times3} & \boldsymbol{0}_{3\times3} & \boldsymbol{0}_{3\times3} & \boldsymbol{0}_{3\times3} \\ \boldsymbol{0}_{3\times3} & \boldsymbol{0}_{3\times3} & \boldsymbol{0}_{3\times3} & -\frac{\boldsymbol{I}_{3*3}}{\boldsymbol{T}_{gb}} & \boldsymbol{0}_{3\times3} & \boldsymbol{0}_{3\times3} & \boldsymbol{0}_{3\times3} & \boldsymbol{0}_{3\times3} & \boldsymbol{0}_{3\times3} \\ \boldsymbol{0}_{3\times3} & \boldsymbol{0}_{3\times3} & \boldsymbol{0}_{3\times3} & \boldsymbol{0}_{3\times3} & -\frac{\boldsymbol{I}_{3*3}}{\boldsymbol{T}_{ab}} & \boldsymbol{0}_{3\times3} & \boldsymbol{0}_{3\times3} & \boldsymbol{0}_{3\times3} & \boldsymbol{0}_{3\times3} \\ \boldsymbol{0}_{3\times3} & \boldsymbol{0}_{3\times3} & \boldsymbol{0}_{3\times3} & \boldsymbol{0}_{3\times3} & \boldsymbol{0}_{3\times3} & -\frac{\boldsymbol{I}_{3*3}}{\boldsymbol{T}_{gs}} & \boldsymbol{0}_{3\times3} & \boldsymbol{0}_{3\times3} & \boldsymbol{0}_{3\times3} \\ \boldsymbol{0}_{3\times3} & \boldsymbol{0}_{3\times3} & \boldsymbol{0}_{3\times3} & \boldsymbol{0}_{3\times3} & \boldsymbol{0}_{3\times3} & \boldsymbol{0}_{3\times3} & -\frac{\boldsymbol{I}_{3*3}}{\boldsymbol{T}_{as}} & \boldsymbol{0}_{3\times3} & \boldsymbol{0}_{3\times3} \\ \boldsymbol{0}_{3\times3} & \boldsymbol{0}_{3\times3} & \boldsymbol{0}_{3\times3} & \boldsymbol{0}_{3\times3} & \boldsymbol{0}_{3\times3} & \boldsymbol{0}_{3\times3} & \boldsymbol{0}_{3\times3} & -\frac{\boldsymbol{I}_{3*3}}{\boldsymbol{T}_{gk}} & \boldsymbol{0}_{3\times3} \\ \boldsymbol{0}_{3\times3} & \boldsymbol{0}_{3\times3} & \boldsymbol{0}_{3\times3} & \boldsymbol{0}_{3\times3} & \boldsymbol{0}_{3\times3} & \boldsymbol{0}_{3\times3} & \boldsymbol{0}_{3\times3} & \boldsymbol{0}_{3\times3} & -\frac{\boldsymbol{I}_{3*3}}{\boldsymbol{T}_{ak}} \end{bmatrix}$$

where $\boldsymbol{\omega}_{in}^n$ represents the angular velocity vector of the navigation frame relative to the inertial frame, $\boldsymbol{C}_b^n$ represents the transformation matrix from the body frame to the navigation frame, $\boldsymbol{f}^b$ represents the output of the accelerometer in terms of specific force, $\boldsymbol{T}_{gb}$ and $\boldsymbol{T}_{ab}$ represent the correlated time constants in modeling the gyroscopes and accelerometers' biases as a first-order Markov model, $\boldsymbol{T}_{gs}$ and $\boldsymbol{T}_{as}$ represent the correlated time constants in modeling the gyroscopes and accelerometers' scale factors as a first-order Markov model, $\boldsymbol{T}_{gk}$ and $\boldsymbol{T}_{ak}$ represent the correlated time constants in modeling the gyroscopes and accelerometers' misalignments as a first-order Markov model.

The state vector is $\boldsymbol{X}_t = \left[\boldsymbol{\varphi}, \delta\boldsymbol{v}, \delta\boldsymbol{p}, \boldsymbol{\varepsilon}^b, \nabla^b, \delta\boldsymbol{K}_g, \delta\boldsymbol{K}_a, \delta\boldsymbol{G}, \delta\boldsymbol{A}\right]_t^T$ .Among these, the vector $\boldsymbol{\varphi}$ represents the attitude angle errors along the East (E), North (N), and Up (U) directions in the local navigation coordinate system, the vector $\delta\boldsymbol{v}$ represents the velocity errors along the E,N,U directions in the local navigation coordinate system, $\delta\boldsymbol{p}$ represents the three-dimensional position error in the geodetic coordinate system, $\boldsymbol{\varepsilon}^b$ and ∇^b represent the biases of the gyroscope and accelerometer along the X, Y, Z directions in the body-fixed coordinate system, $\delta\boldsymbol{K}_g$ and $\delta\boldsymbol{K}_a$ represent scale factor coefficients of the gyroscope and accelerometer along the X, Y, Z directions in the body-fixed coordinate system, and $\delta\boldsymbol{G}$ and $\delta\boldsymbol{A}$ represent misalignment coefficients of the gyroscope and accelerometer along the X, Y, Z directions in the body-fixed coordinate system.

The noise vector of the system is as follows:

$$\boldsymbol{W}_t = \left[\boldsymbol{w}_{rg}, \boldsymbol{w}_{ra}, 0_{1*3}, \boldsymbol{w}_{gb}, \boldsymbol{w}_{ab}, \boldsymbol{w}_{gs}, \boldsymbol{w}_{as}, \boldsymbol{w}_{gk}, \boldsymbol{w}_{ak}\right]_t^T \quad (7)$$

where $\boldsymbol{w}_{rg}$ and $\boldsymbol{w}_{ra}$ represent the random white noise of the gyroscope and accelerometer, $\boldsymbol{w}_{gb}$ and $\boldsymbol{w}_{ab}$ represent the driving noises of the gyroscope bias and accelerometer bias, $\boldsymbol{w}_{gs}$ and $\boldsymbol{w}_{as}$ represent the driving noises of the gyroscope scale factor and accelerometer scale factor, and $\boldsymbol{w}_{gk}$ and $\boldsymbol{wak}$ represent the driving noises of the gyroscope misalignment and accelerometer misalignment.

The measurement equation of calibration

The SINS/LBL filter corrects the system state vector using the measurement equation. The observation vector for LBL is the distance between the vehicle and the seafloor beacon. During the measurement update, the observation innovation is obtained by subtracting the observed value calculated by SINS from the actual observation value. The measurement equation for the tightly coupled SINS/LBL integrated navigation system is as follows:

$$\boldsymbol{Z}_t = \begin{bmatrix} \boldsymbol{\rho}_{1,t}^{\mathrm{SINS}} - \boldsymbol{\rho}_{1,t}^{\mathrm{LBL}} \\ \cdots \\ \boldsymbol{\rho}_{i,t}^{\mathrm{SINS}} - \boldsymbol{\rho}_{i,t}^{\mathrm{LBL}} \end{bmatrix} = \boldsymbol{H}_t\boldsymbol{X}_t + \boldsymbol{V}_t \quad (8)$$

where $\boldsymbol{\rho}_{i,t}^{\mathrm{SINS}}$ represents the distance between the ith seafloor beacon and the IMU sensor calculated by SINS at time t, $\boldsymbol{\rho}_{i,t}^{\mathrm{LBL}}$ represents the distance between the ith seafloor beacon and the transducer observed at time t.

$\boldsymbol{H}_t$ represents the measurement update matrix, and its expression is as follows:

$$\boldsymbol{H}_t = \begin{bmatrix} -\boldsymbol{E}_{1,t}\boldsymbol{C}_g^n\boldsymbol{M}_{pv,t}\left(\boldsymbol{C}_{b,t}^n\delta\boldsymbol{l}^b\right)\times & \boldsymbol{0}_{1\times3} & -\boldsymbol{E}_{1,t}\boldsymbol{C}_g^n & \boldsymbol{0}_{1\times18} \\ & \cdots & & \\ -\boldsymbol{E}_{i,t}\boldsymbol{C}_g^n\boldsymbol{M}_{pv,t}\left(\boldsymbol{C}_{b,t}^n\delta\boldsymbol{l}^b\right)\times & \boldsymbol{0}_{1\times3} & -\boldsymbol{E}_{i,t}\boldsymbol{C}_g^n & \boldsymbol{0}_{1\times18} \end{bmatrix} \quad (9)$$

where $\boldsymbol{E}_{i,t} = \begin{bmatrix} \frac{\partial\boldsymbol{\rho}_{i,t}^{\mathrm{SINS}}}{\partial x} \\ \frac{\partial\boldsymbol{\rho}_{i,t}^{\mathrm{SINS}}}{\partial y} \\ \frac{\partial\boldsymbol{\rho}_{i,t}^{\mathrm{SINS}}}{\partial z} \end{bmatrix}^T$, $\boldsymbol{C}_g^n = \boldsymbol{C}_e^n\boldsymbol{C}_g^e$,

$$\boldsymbol{C}_e^n = \begin{bmatrix} -\sin\lambda & -\sin L\cos\lambda & \cos L\cos\lambda \\ \cos\lambda & -\sin L\sin\lambda & \cos L\sin\lambda \\ 0 & \cos L & \sin L \end{bmatrix}^T,$$

$$\boldsymbol{C}_g^e = \begin{bmatrix} -(R_N+h)sinLcos\lambda & -(R_N+h)\cos L\sin\lambda & \cos L\cos\lambda \\ -(R_N+h)\sin L\sin\lambda & (R_N+h)\cos L\cos\lambda & \cos L\sin\lambda \\ \left(R_N\left(1-a^2\right)+h\right)\cos L & 0 & \sin L \end{bmatrix},$$

$$\boldsymbol{M}_{pv,t} = \begin{bmatrix} 0 & \frac{1}{(R_M+h)} & 0 \\ \frac{1}{(R_N+h)\cos L} & 0 & 0 \\ 0 & 0 & 1 \end{bmatrix}.$$

R_N represents the curvature radius of the meridian circle at vehicle position, R_M represents the curvature radius of the prime vertical circle at vehicle position, h represents the elevation, L represents the latitude at time t, λ represents the longitude at time t, $\boldsymbol{C}_{b,t}^n$ represents the coordinate rotation matrix from the body-fixed coordinate system to the local navigation coordinate system at time t, $\delta\boldsymbol{l}^b$ represents the lever arm between the IMU sensor and the transducer, a represents the first eccentricity of the Earth, $\boldsymbol{V}_t = \left[v_{1,t}^p, \cdots, v_{i,t}^p\right]^T$ represents the measurement noise vector,$v_{i,t}^p$ represents the distance error between the ith seafloor beacon and the transducer

at time t, b represents the body-fixed coordinate system,n represents the local navigation coordinate system,g represents the geodetic coordinate system, and e represents the Earth-centered, Earth-fixed coordinate system.

The feedback of calibration

Discretizing the state equation and measurement equation given by Eqs. (6) and (8), the state update process of the filter is as follows:

$$\begin{aligned} \boldsymbol{X}_{k+1/k} &= \boldsymbol{F}_{k+1/k}\boldsymbol{X}_k \\ \boldsymbol{P}_{k+1/k} &= \boldsymbol{F}_{k+1/k}\boldsymbol{P}_k\boldsymbol{F}_{k+1/k}^T + \boldsymbol{Q}_k \end{aligned} \tag{10}$$

the measurement update process of the filter is as follows:

$$\begin{aligned} \boldsymbol{K}_{k+1} &= \boldsymbol{P}_{k+1/k}\boldsymbol{H}_{k+1}^T(\boldsymbol{H}_{k+1}\boldsymbol{P}_{k+1/k}\boldsymbol{H}_{k+1}^T + \boldsymbol{R}_{k+1})^{-1} \\ \boldsymbol{X}_{k+1} &= \boldsymbol{X}_{k+1/k} + \boldsymbol{K}_{k+1}(\boldsymbol{Z}_{k+1} - \boldsymbol{H}_{k+1}\boldsymbol{X}_{k+1/k}) \\ \boldsymbol{P}_{k+1} &= (\boldsymbol{I} - \boldsymbol{K}_{k+1}\boldsymbol{H}_{k+1})\boldsymbol{P}_{k+1/k} \end{aligned} \tag{11}$$

where, $\boldsymbol{X}_k$, $\boldsymbol{X}_{k+1/k}$, and $\boldsymbol{X}_{k+1}$ represent the estimated state vector at time K, the prediction state vector, and the estimated state vector at time $K+1$, respectively. $\boldsymbol{P}_k$, $\boldsymbol{P}_{k+1/k}$, and $\boldsymbol{P}_{k+1}$ represent the error covariance matrix of the state variable at time K, the prediction error covariance matrix, and the error covariance matrix of the state variable at time $K+1$, respectively. $\boldsymbol{Q}_k$ represents the system noise matrix. $\boldsymbol{F}_{k+1/k}$ represents the state transition matrix. $\boldsymbol{K}_{k+1}$, $\boldsymbol{H}_{k+1}$, $\boldsymbol{R}_{k+1}$, and $\boldsymbol{Z}_{k+1}$ represent the Kalman filter gain matrix, measurement update matrix, observation noise matrix, and observation innovation, respectively.

The error feedback model is as follows:

$$\left.\begin{aligned} \boldsymbol{\omega}_{ib}^b &= \left[\boldsymbol{I} - \delta\boldsymbol{K}_g - \delta\boldsymbol{G}\right]\left(\tilde{\boldsymbol{\omega}}_{ib}^b - \boldsymbol{\varepsilon}^b\right) \\ \boldsymbol{f}^b &= \left[\boldsymbol{I} - \delta\boldsymbol{K}_a - \delta\boldsymbol{A}\right]\left(\tilde{\boldsymbol{f}}^b - \nabla^b\right) \end{aligned}\right\} \tag{12}$$

$\tilde{\boldsymbol{\omega}}_{ib}^b$ and $\tilde{\boldsymbol{f}}^b$ represent the measurement outputs of the gyroscope and accelerometer, respectively.

In Eq. (11), $\boldsymbol{X}_{k+1}$ and the error covariance matrix $\boldsymbol{P}_{k+1}$ are estimated. As the filter continues to update for a certain period, the error covariance matrix $\boldsymbol{P}_{k+1}$ gradually tends towards zero, which implies that the estimated state vector $\boldsymbol{X}_{k+1}$ approaches the true value. Substituting this value into Eq. (12) yields the theoretical outputs $\boldsymbol{w}_{ib}^b$ and $\boldsymbol{f}^b$ of the gyroscope and accelerometer.

Experimental results and analysis

Experimental scenarios and data sources

The experimental data used in the study were obtained from a shallow sea experiment conducted on Lingshan Island, Qingdao, Shandong Province on August 24, 2022.

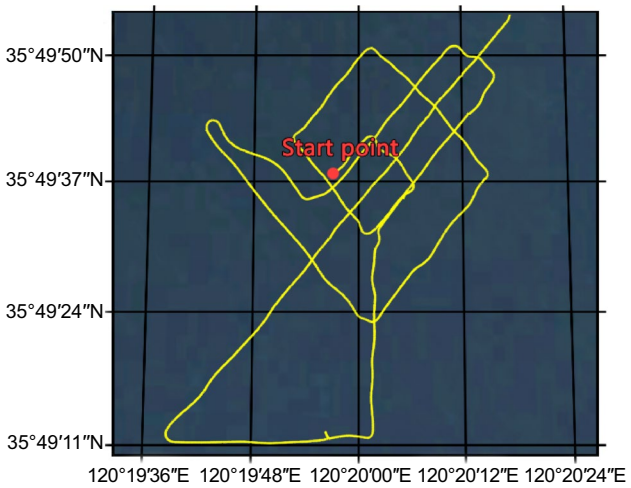

Fig. 2 Actual track line of the experimental vessel

The experimental area is depicted in Fig. 2, where the actual track line of the experimental vessel is presented. Five acoustic beacons were installed on the seafloor, and acoustic transducers were mounted on the bottom of the test vessel to receive the signals from the seafloor beacons. Additionally, the test vessel was equipped with a GNSS receiver, a Micro-Electro Mechanical Systems (MEMS)-grade IMU EPSON G370, and a tactical-grade IMU XW-G17660-v2.1, as illustrated in Fig. 3.

Table 1 shows the primary performance parameters of the EPSON G370. The gyroscope bias and accelerometer bias of the XW-G17660-v2.1 are 0.3 (°)/h and 1×10^{-6} m/s^2, respectively. The measurement update frequency of transducer is 0.5 Hz, and the IMU update frequency is 100 Hz. Note that the sea surface vessel is used as "underwater vehicle" in the study. Though the test vessel is equipped with GNSS receiver, it is neither combined with the acoustic measurement nor the inertial measurement. The GNSS position is used as the reference to validate the positioning accuracy based on the acoustic-based and inertial-based positioning results.

In order to calibrate the IMU sensor using acoustic signals, the study conducted both simulation and field experiments. In the simulation experiment, the IMU errors can be pre-set and used as the evaluation criteria for calibration accuracy. In the field experiment, it is not possible to obtain the true IMU error parameters in advance. Therefore, assessing the quality of calibration results directly is not feasible. In such cases, the calibrated error parameters can be fed back to the SINS. The time taken for SINS Three Dimensional (3D) position error to diverge by 1 km can be used as an indicator to evaluate the calibration accuracy.

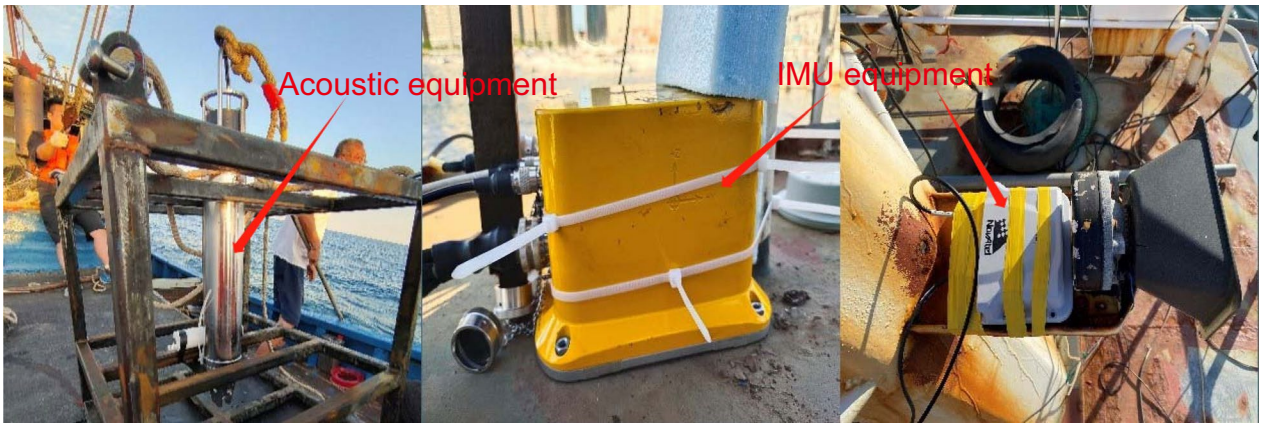

Fig. 3 Acoustic and IMU equipment used in the experiment

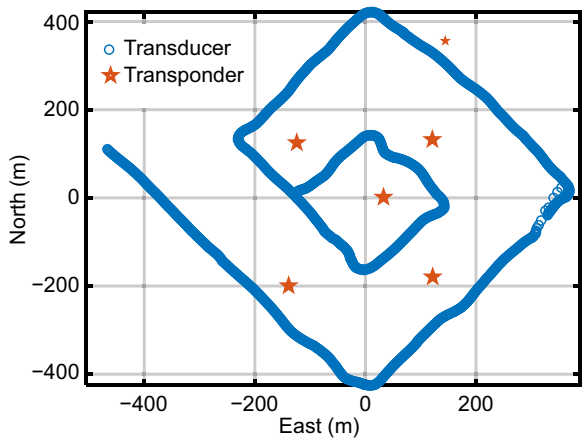

Fig. 4 The trajectory of test vehicle and locations of the seafloor beacons

The performance analysis of acoustic navigation

Before using acoustic signals to calibrate IMU errors online, an analysis of the acoustic navigation performance was performed. The GNSS Real-Time Kinematic (RTK) was used to calculate the position of the onboard GNSS receiver, which was then adjusted to the position of the transducer at the bottom of the vessel using the lever arm, serving as a reference to obtain the acoustic navigation position error. In Fig. 4, the blue spiral line represents the measured vessel's trajectory, while the red stars indicate the five pre-deployed seafloor beacons. As the measuring vessel progresses, the transducer located at the vessel's bottom receives the acoustic signals from the seafloor beacons. Given the coordinates of the seafloor beacons, the position of the transducer can be calculated.

Comparing the acoustic navigation position with the reference position of the transducer determined by GNSS, the position error of acoustic navigation can be obtained, as shown in Fig. 5.

From Fig. 5, we can see that the overall navigation error in the E direction is less than 2 m inside the network and less than 6 m outside the network. In the N direction, the overall navigation error is less than 2 m inside the network and less than 4 m outside the network. In the U direction, with the constraints of pressure gauges, the overall navigation error is less than 1 m inside the network and less than 2 m outside the network. In detail, the Root Mean Square (RMS) error for the acoustic navigation during the spiral track is 1.68, 1.34, 0.38 m in the E,N,U direction, respectively.

Due to the cumulative error of SINS, the position error will reach approximately 1000 m within a certain period. Taking MEMS-grade IMU as an example and assuming the bias of 36.8 (°)/h, the cumulative position error can theoretically reach 1 000 m within 126 s. Therefore, in the underwater environment the meter-level acoustic navigation is attainable because the IMU can be calibrated to a

Table 1 Main performance parameters of EPSON G370

Sensor	Parameters	EPSON G370
Accelerometer	Repeatability	2×10^{-5} m/s^2
	In-run bias stability	1×10^{-7} m/s^2
	Scale factor	1‰
	Misalignment	0.01°
	Velocity random walk	0.025 m/(s·h$^{1/2}$)
Gyroscope	Repeatability	0.01 (°)/s
	In-run bias stability	0.8 (°)/h
	Scale factor	1‰
	Misalignment	0.01°
	Angular random walk	0.06 (°)/h$^{1/2}$

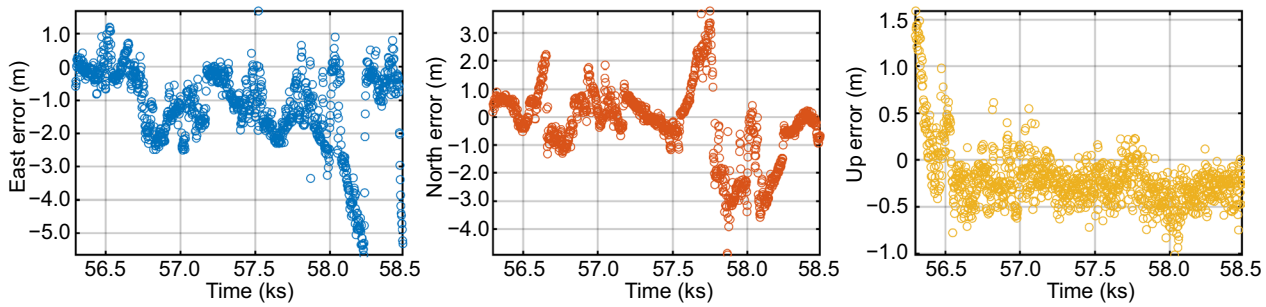

Fig. 5 Acoustic navigation error in the ENU direction during the experiment

certain accuracy level, which improves the navigation accuracy of SINS.

Accuracy improvement with different types of calibration parameters

The observability of the IMU errors, such as the scale factor and misalignment, is generally low when the underwater vehicle maneuverability is weak (Paull et al., 2018). Accurate calibration of such errors typically requires complex maneuvers such as climbing and rolling, which is often challenging for underwater vehicles. In this section, we employ simulation methods to study the impact of different types of IMU errors on the divergence of SINS position error.

The experiment simulated five different scenarios: without feedback of IMU errors, with feedback of scale factor, with feedback of misalignment, with feedback of bias, and with feedback all the three types of IMU errors. The simulation was based on the EPSON G370 IMU parameters used in the experiment with the following paraments: gyroscope bias of 36.8 (°)/h, accelerometer bias of 2×10^{-5} m/s^2, gyroscope scale factor of 1‰, accelerometer scale factor of 1‰, gyroscope misalignment of 1.74×10^{-4}, and accelerometer misalignment of 1.74×10^{-4}. The results are presented in Table 2.

Comparing the scheme without feedback of IMU errors and the scheme with feedback of bias, the time taken for SINS position error to reach 1 km is longer by 33.97 s. This accounts for 95.6% of the total improvement time, which indicates that the main error accumulation of the SINS is caused by the biases of gyroscope and accelerometer. Therefore, accurate calibration of these biases can not only reduce the complexity of the calibration model, but also effectively suppress the rate of SINS error divergence.

Table 2 The performance of the feedback of different types of IMU errors

Type of feedback error	Scale factor	Misalignment	Bias	All
Improvement time (s)	0.60	0.95	33.97	35.54
Percentage of total improvement time	1.70%	2.70%	95.60%	100%

Accuracy improvement with different calibration trajectories

Simulation experiment on the influence of different calibration trajectories

To investigate the impact of different calibration trajectories on the accuracy and convergence speed of IMU calibration using acoustic signal, the experiment simulated seven cases: straight and diamond-shaped calibration trajectories with and without the change in depth, and three sets of curve calibration trajectories with the change in depth: circular, S-shaped, and figure-eight trajectories as presented in Figs. 6 and 7.

The simulated IMU parameters were gyroscope bias of 36.8 (°)/h and accelerometer bias of 2×10^{-5} m/s^2. The convergence process of gyroscope bias and accelerometer bias along with their covariance matrices for the simulated straight and diamond-shaped calibration trajectories with and without the changes in depth are shown in Figs. 8 and 9.

From Figs. 8 and 9, we can see that for both the straight and diamond-shaped calibration trajectories, the performances for the trajectories with the change in depth outperform those without the change in depth, particularly in the U direction of the gyroscope bias. From the shaded areas in Figs. 8 and 9, it can be observed that the change in depth enhances the convergence speed of gyroscope bias in the U direction, improving the calibration effect of gyroscope bias in the U direction. The exact calibration results of gyroscope bias and accelerometer bias are presented in Table 3.

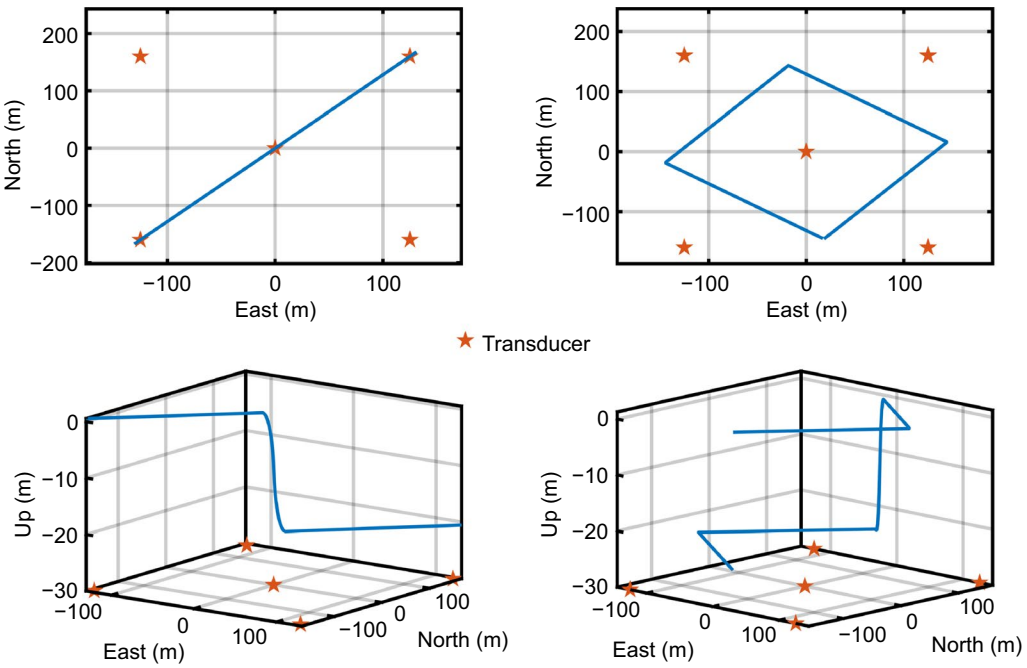

Fig. 6 The simulated straight (Left) and diamond-shaped (Right) calibration trajectories without(top) and with(bottom) the change in depth in the experiment

Comparing Figs. 8 and 9, together with Table 3, we can see that for both the trajectories with and without depth variation, the calibrated gyroscope bias and accelerometer bias from the diamond-shaped trajectory are closer to the preset biases than those from the straight trajectory.

As shown in Fig. 6, the diamond-shaped includes turning maneuvers, which is different from the straight. To discover the reason for the different performance of the straight and diamond-shaped trajectories, an observability analysis was conducted for gyroscope bias and accelerometer bias during uniform straight-line maneuver and turning maneuver. The analysis results are shown in Fig. 10. It is noted that to stand out the advantage of the turning maneuver trajectory, the depth variations are not simulated in Fig. 10 of the observability analysis.

From Fig. 10, we can see that comparing to the straight calibration trajectory, the observability of gyroscope bias in the U direction and accelerometer biases in the E and N directions improves when turning maneuvers are present. For the straight trajectory only with uniform straight-line maneuver, the observability of gyroscope bias in the U direction is quite weak due to the lack of the depth variations. We find that the diamond-shaped trajectory with turning maneuver can improve the observability of the gyroscope bias in the U direction significantly. In fact, when the effects of depth variations are taken into consideration, like the turning maneuvers, the observability of gyroscope bias in the U direction can be improved. However, in the case of the observability of accelerometer bias, the situation is different. For the straight calibration trajectory only with uniform straight-line maneuver, the observability of accelerometer biases in the E and N directions is weak and can be improved with the turning maneuvers, which is consistent with the experimental results in Table 3. It is noted that due to the gravity excitation, the observability of accelerometer bias in the U direction is always strong for both the uniform straight-line maneuver and the turning maneuver. Therefore, the observability analysis in Fig. 10 highlights the advantages of the turning maneuvers for the calibration of the gyroscope bias and accelerometer bias.

Furthermore, to figure out the optimal calibration trajectory, we simulate three more sets of curve trajectories and try to find the mechanism for the optimal trajectory design. Since the depth variation has been proved to be important for the gyroscope bias and accelerometer bias calibration, all the three trajectories consider the depth variations, as presented in Figs. 11 and 12.

Figures 11 and 12 represent the convergence process of gyroscope bias and accelerometer bias with the circular, S-shaped and the figure-eight calibration trajectories, respectively. The accuracy of calibrated gyroscope bias and accelerometer bias for these three trajectories are presented in Table 4.

Comparing Table 4 with Table 3, for the circular, S-shaped, and figure-eight calibration trajectories, the

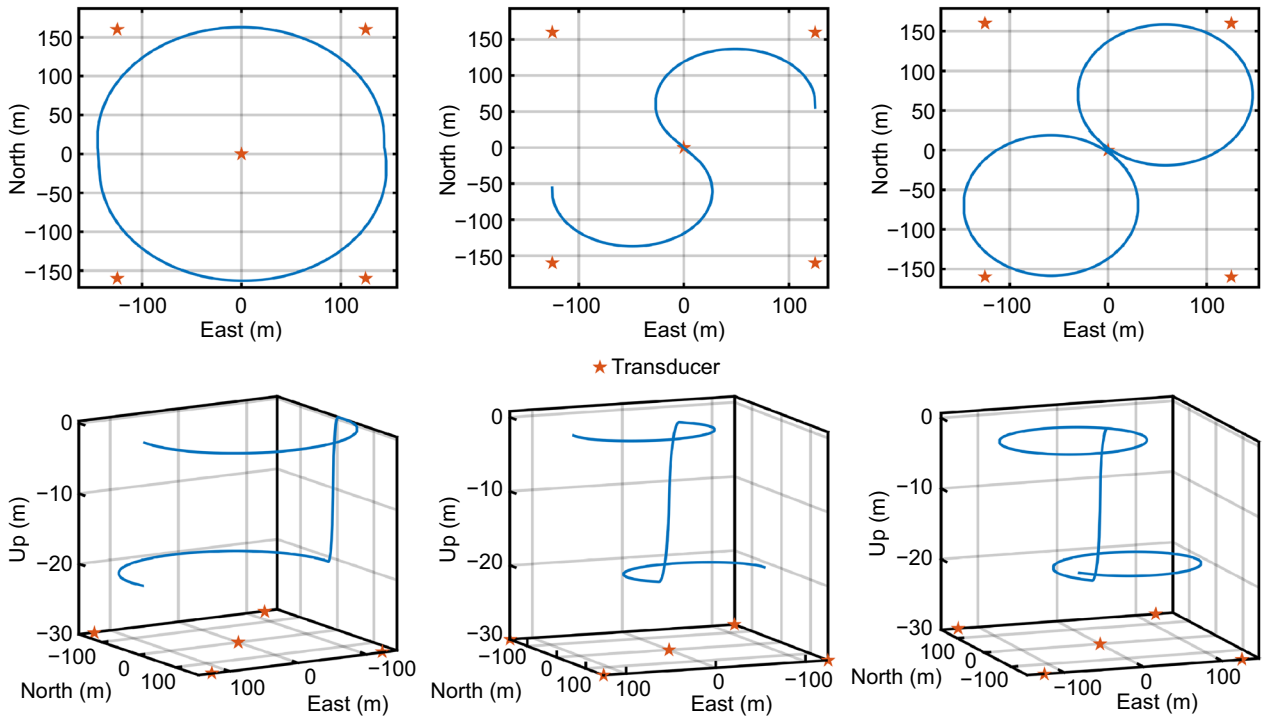

Fig. 7 Top-view and three-dimensional figures of the circular (Left), S-shape(Middle) and figure-eight (Right) calibration trajectories

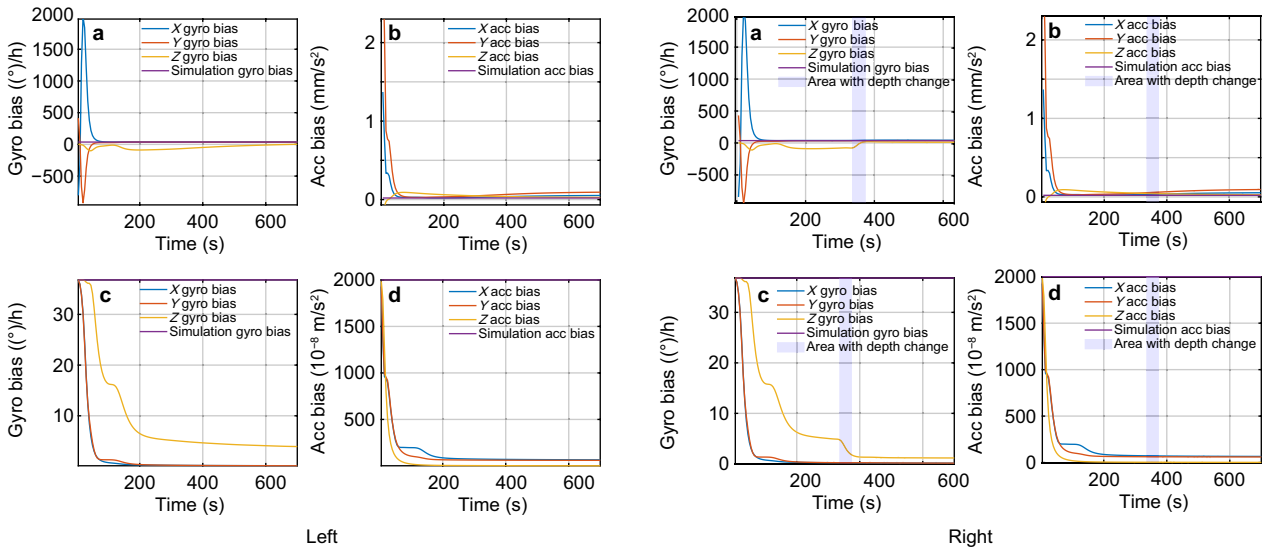

Fig. 8 The convergence process of gyroscope bias (**a**) and accelerometer bias (**b**) along with their covariance matrices (**c**) and (**d**) of straight calibration trajectory without the change in depth (Left) and with the change in depth (Right)

calibration results surpass those of the straight and diamond-shaped calibration trajectory. This is primarily attributed to the turning maneuvers present in the curve calibration trajectories. Among these three trajectories, the calibration performance for the figure-eight trajectory stands out as the most optimal. The major difference among these three trajectories lies in their respective observation structures. We separately calculated the Position Dilution Of Precision (PDOP) values at each moment for the circular, S-shaped, and

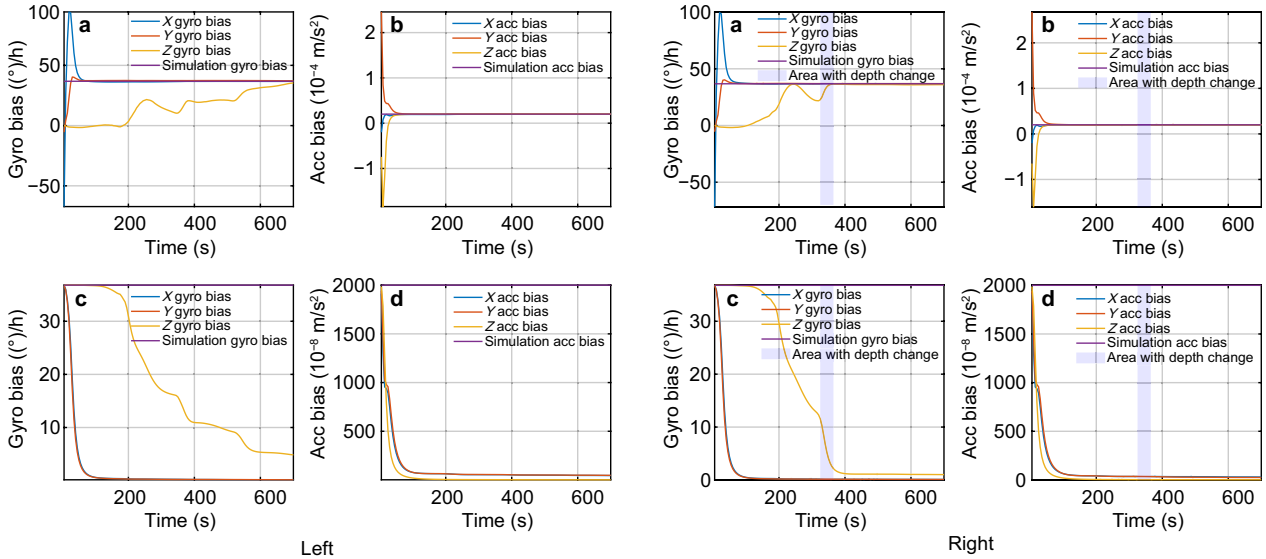

Fig. 9 The convergence process of gyroscope bias (**a**) and accelerometer bias (**b**) along with their covariance matrices (**c**) and (**d**) of diamond-shaped calibration trajectory without the change in depth (Left) and with the change in depth (Right)

figure-eight trajectories. The results show that the average PDOP value for the circular trajectory is 5.5498, for the S-shaped trajectory is 4.5029, and for the figure-eight trajectory is 4.2666. This indicates that the figure-eight calibration trajectory possesses a better observation structure, resulting in the optimal acoustic calibration of the inertial navigation.

Lastly, in the study, we define the calibration convergence by the time taken for the IMU errors in the covariance matrices to converge to 10% of the preset error. Therefore, from Figs. 8 and 9, it can be observed that comparing the straight trajectory with and without the change in depth, as well as the diamond-shaped with and without the change in depth, it is clear that the convergence speed for the gyroscope bias in the *U* direction is faster when depth variations are considered, than those without considering depth changes. From Figs. 11 and 12 of three curve trajectories, the convergence speed for the gyroscope bias in the *U* direction remains approximately consistent. Comparing Figs. 11 and 12 with Figs. 8 and 9, the convergence speeds of these curve trajectories for the gyroscope bias in the *U* direction are slightly lower than those of the straight and diamond-shaped trajectory with the change in depth. In addition, the convergence speed of gyroscope biases in the *E* and *N* directions and the accelerometer biases in the *E*, *N* and *U* directions are generally comparable for these seven calibration trajectories.

Field experiment on the influence of different calibration trajectories

In order to further verify the results of the above simulation experiment, a field experiment was conducted based on the data obtained in Qingdao shallow sea experiment on August 24, 2022. Firstly, based on the measured data from the test vessel, only the data for straight and diamond-shaped trajectory without the change in depth is available. On the other hand, the calibration trajectory practically needs balancing between complexity and operability. Therefore, in this experiment, a comparison is made between the calibration effects for the straight and diamond-shaped trajectories without the change in depth. The results are illustrated in Figs. 13 and 14.

From Figs. 13 and 14, it can be observed that the convergence speeds of calibrated gyroscope bias and accelerometer bias for both the straight and diamond-shaped trajectories are consistent with the simulation results. In terms of calibration accuracy, the calibration results for IMU errors using the straight and diamond-shaped trajectories are presented in Table 5.

Since it is impossible to obtain the true gyroscope and accelerometer biases in advance during the field experiment, it is not possible to directly determine which calibration result has higher accuracy. In this study, the biases obtained from the straight and diamond-shaped trajectories are separately fed back into SINS. The time taken for the SINS position error to reach 1 km is used as the indicator to measure the accuracy of each calibration. The results after the feedback are shown in Fig. 15. The maintenance time for the diamond-shaped trajectory

Table 3 Calibration results of gyroscope bias and accelerometer bias for the straight and diamond-shaped trajectories in the simulation experiment

Project	ε_x^b((°)/h)	ε_y^b((°)/h)	ε_z^b((°)/h)	$\nabla_x^b(10^{-8}\,m/s^2)$	$\nabla_y^b\,(10^{-8}\,m/s^2)$	$\nabla_z^b\,(10^{-8}\,m/s^2)$
Preset bias	36.8	36.8	36.8	2000	2000	2000
Bias of straight trajectory	36.8	35.39	−3.47	5187	9385	2041
Bias of diamond-shaped trajectory	36.8	36.68	35.89	1967	2023	2004
Bias of straight trajectory with depth	36.8	37.45	31.36	3579	6841	2027
Bias of diamond-shaped trajectory with depth	36.8	36.94	36.03	1981	2017	2003

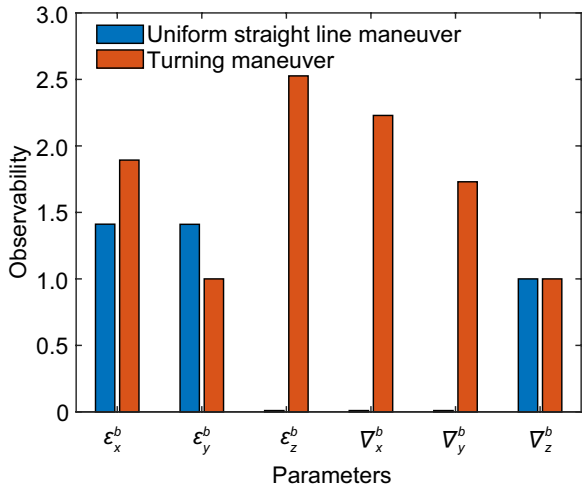

Fig. 10 Observability of gyroscope bias and accelerometer bias

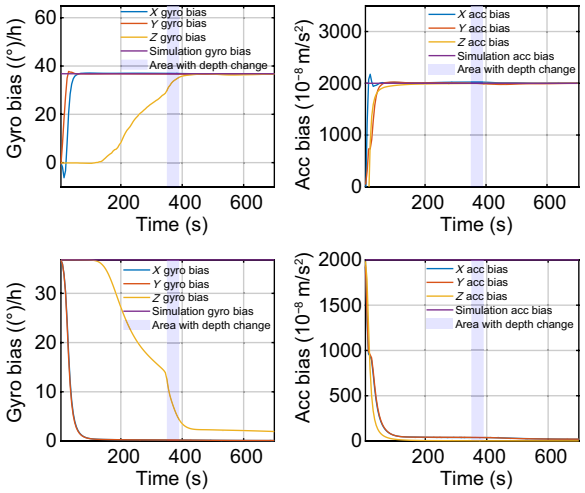

Fig. 12 The convergence process of gyroscope bias (**a**) and accelerometer bias (**b**) along with their covariance matrices (**c**) and (**d**) of figure-eight calibration trajectory

is 239 s, while that for the straight-line trajectory is 200 s.

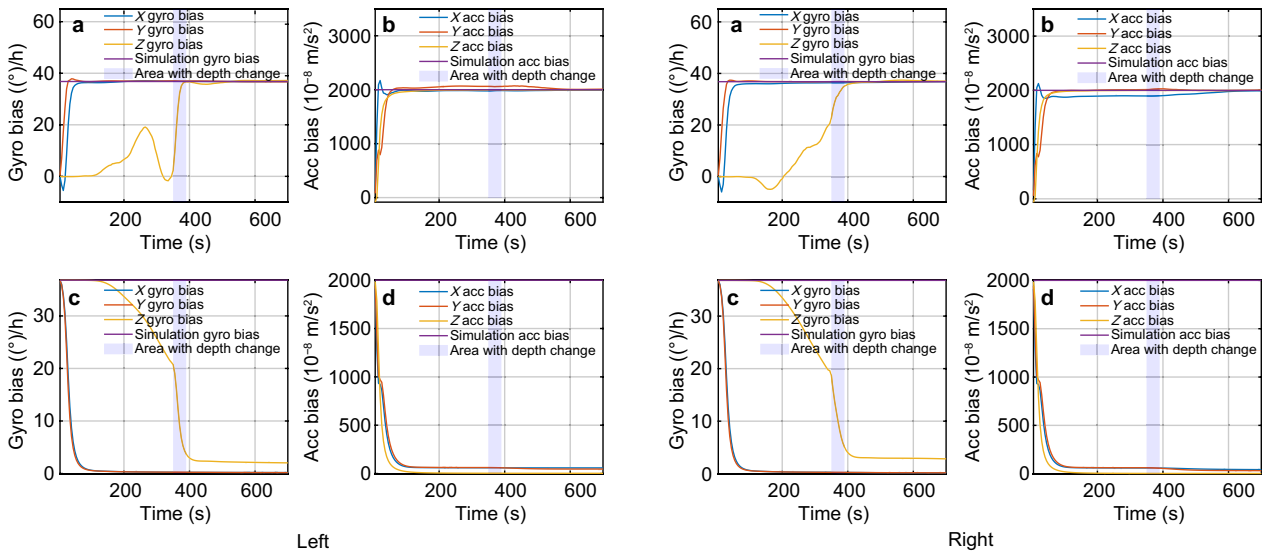

Fig. 11 The convergence process of gyroscope bias (**a**) and accelerometer bias (**b**) along with their covariance matrices (**c**) and (**d**) of circular calibration trajectory(Left) and S-shaped calibration trajectory(Right)

Table 4 Calibration results of gyroscope bias and accelerometer bias for the three sets of curve calibration trajectories in the simulation experiment

Project	$\varepsilon_x^b((°)/h)$	$\varepsilon_y^b((°)/h)$	$\varepsilon_y^b((°)/h)$	$\nabla_x^b(10^{-8}\,m/s^2)$	$\nabla_y^b(10^{-8}\,m/s^2)$	$\nabla_z^b(10^{-8}\,m/s^2)$
Preset bias	36.8	36.8	36.8	2000	2000	2000
Bias of circular trajectory	36.8	36.68	37.19	1990	2010	1998
Bias of S-shaped trajectory	36.8	36.91	36.94	1991	2007	2001
Bias of figure-eight trajectory	36.8	36.70	36.73	2004	1998	2000

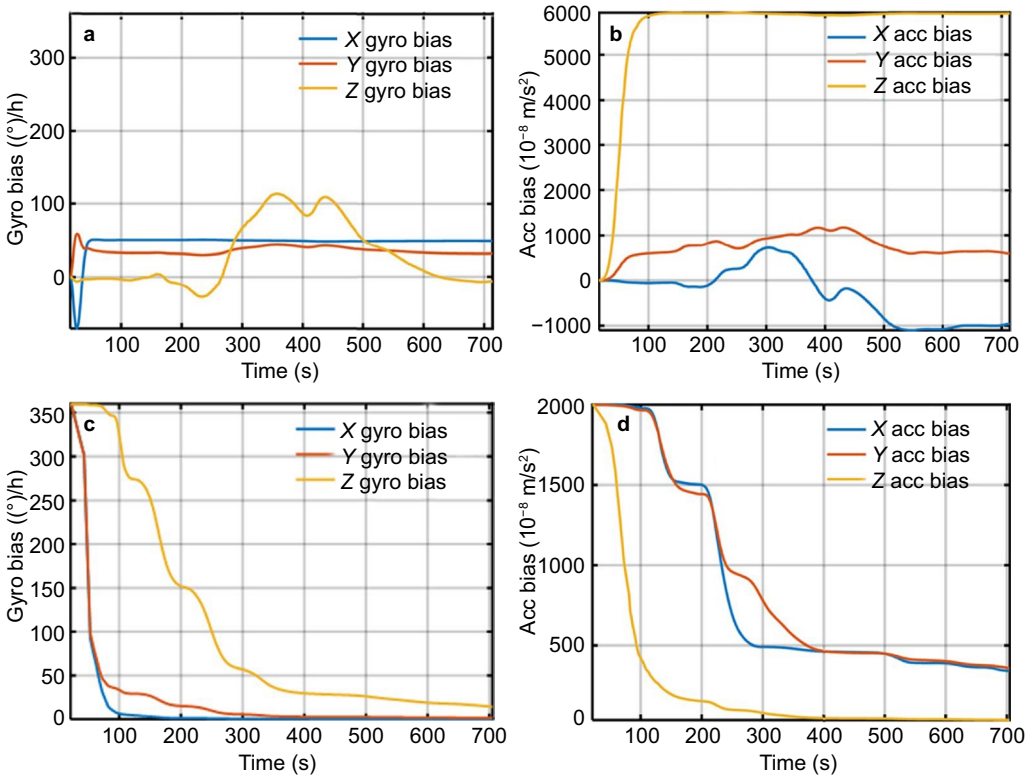

Fig. 13 The convergence process of gyroscope bias (**a**) and accelerometer bias (**b**) along with their covariance matrices (**c**) and (**d**) with straight calibration trajectory without the change in depth in the field experiment

Therefore, it can be inferred that the calibration using the diamond-shaped trajectory achieves higher calibration accuracy, which is consistent with the results of the simulation experiment.

Accuracy improvement with different precision IMU

Due to the different error accumulation characteristics of different grade IMU, the effectiveness of acoustic-based IMU online-calibration may differ. Therefore, this section primarily analyzes the impact of different-grade IMU on the calibration. The data used in the analysis is from Qingdao shallow sea experiment conducted on August 24, 2022, which included a MEMS-grade and a tactical-grade IMU. The MEMS-grade IMU has a gyroscope bias of 36.8 (°)/h, while the tactical-grade IMU has a gyroscope bias of 0.3 (°)/h. The calibration was performed separately for both systems, and the results were fed back into the SINS. The time taken for SINS position error to reach 1 km and the corresponding improvements are presented in Fig. 16 and Table 6.

The results indicate that compared to the case without feedback, the MEMS-grade IMU shows a 38.9% improvement in maintenance time after the feedback of the laboratory bias and a 121% improvement after the feedback of the acoustic-based online calibration bias. On the other hand, the tactical-grade IMU exhibited a 1% improvement in maintenance time after the feedback of the

Table 5 Calibration results of gyroscope bias and accelerometer bias in the field experiment

Items	ε_x^b((°)/h)	ε_y^b((°)/h)	ε_z^b((°)/h)	∇_x^b (10^{-8} m/s^2)	∇_y^b (10^{-8} m/s^2)	∇_z^b (10^{-8} m/s^2)
Bias of straight trajectory	49.3	31.7	−6.21	−872.8	644.8	5915
Bias of diamond-shaped trajectory	49.5	44.2	62.9	628.6	773.1	5982

Table 6 The percentage increase in maintenance time compared to the case without feedback

Items	Laboratory bias (%)	Online-calibration bias (%)
MEMS-grade IMU	38.9	121.0
Tactical-grade IMU	1.0	56.9

laboratory bias and a 56.9% improvement after the feedback of the acoustic-based calibration bias.

From the above results, it can be found that acoustic-based calibration for low-grade IMU has a more significant impact on improving the position accuracy than high-grade one. This may be caused by the factor that high-grade IMU exhibits slower error divergence rates; therefore, the percentage improvement is not as significant as low-grade IMU. Comparing the feedback of the laboratory bias with the feedback of the acoustic-based calibration bias, the latter has a greater effect on suppressing the rate of error divergence of SINS. This may be caused by the factor that gyroscopes have a temperature-dependent bias known as thermal bias, which represents the change in bias value relative to the room temperature bias within the specified operating temperature range. Therefore, the acoustic-based calibration bias can better reflect the actual bias during inertial navigation experiments.

Conclusion

High-precision underwater navigation is a prerequisite for underwater vehicles to explore the marine environment and resources and to conduct deep-sea scientific research and deep-sea engineering operations. To provide long-term and high-precision underwater navigation for an underwater vehicle, we proposed an acoustic LBL-based IMU calibration algorithm and analyzed the impacts of different types of calibration parameters, different calibration trajectories, and different-grade IMUs on the underwater navigation accuracy improvement. The conclusions are as follows.

(1) The acoustic LBL-based IMU online calibration model is presented in detail. We presented the model of IMU errors, the state equation of calibration, and especially the measurement equation of calibration. In the measurement equation for the tightly coupled SINS/LBL integrated navigation system, the observation innovation is obtained by subtracting the distance between the seafloor beacon and the IMU sensor calculated by SINS as well as the distance between the seafloor beacon and the transducer.

(2) We analyzed the impacts of different IMU error parameters on the calibration accuracy of IMU using acoustic signals. Taking the EPSON G370 IMU parameters as an example, experiments simulate the impact of three main types of IMU errors on error divergence. The results demonstrate that the bias has a predominant effect on error divergence, accounting for as much as 95.6% of the total effects.

(3) We analyzed the impacts of different calibration trajectories on the calibration accuracy of IMU using acoustic signals. We find that an optimal calibration trajectory needs to consider the effects of the three-dimensional observability and PDOP. In the experiment, we compared the calibration effects of seven calibration trajectories: straight trajectory with and without the change in depth, diamond-shaped trajectory with and without the change in depth, and three curve trajectories with the change in depth: the circular, S-shaped, and figure-eight trajectory. Among them, we find that the figure-eight trajectory is the optimal one for acoustic LBL-based IMU online calibration.

(4) Finally, the impacts of different-grade IMU on the calibration accuracy of IMU using acoustic signals are presented. The experimental data from both MEMS-grade and tactical-grade IMU were analyzed. The experiment shows that acoustic calibration has a more pronounced effect on improving the accuracy of low-grade IMU compared to high-grade one. For the MEMS-grade IMU sensor, the maintenance time of the IMU calibrated by the proposed algorithm can increase by 121% compared to the IMU without calibration while that by the laboratory default calibration parameter can increase by

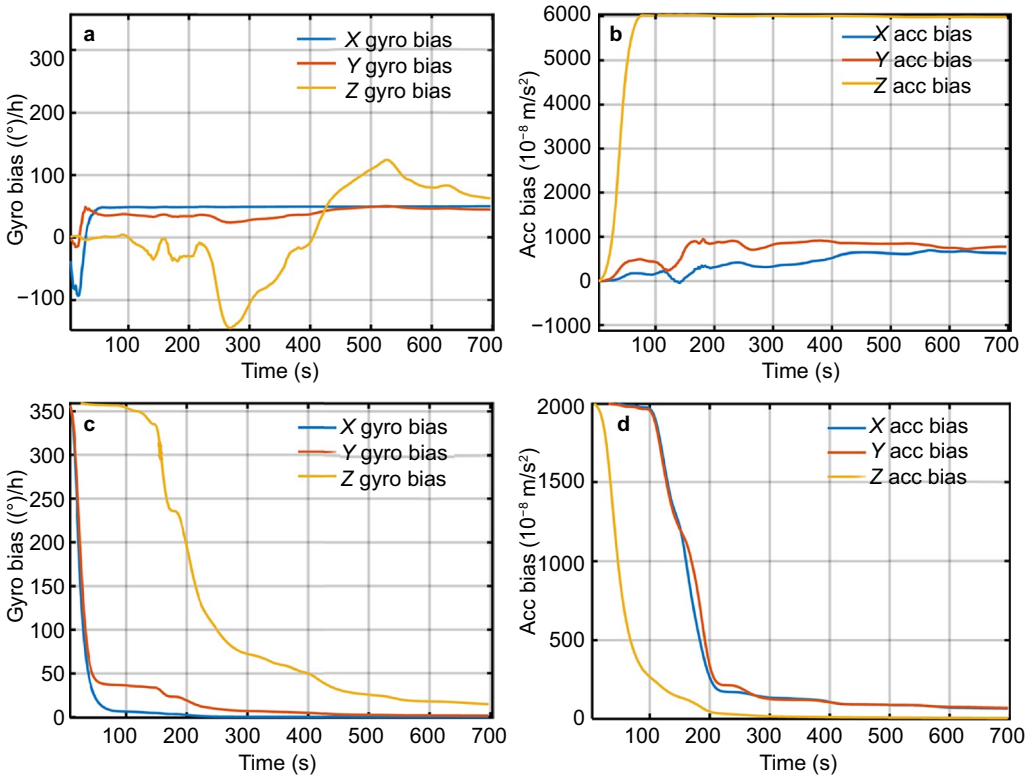

Fig. 14 The convergence process of gyroscope bias (**a**) and accelerometer bias (**b**) along with their covariance matrices (**c**) and (**d**) with diamond-shaped calibration trajectory without the change in depth in the field experiment

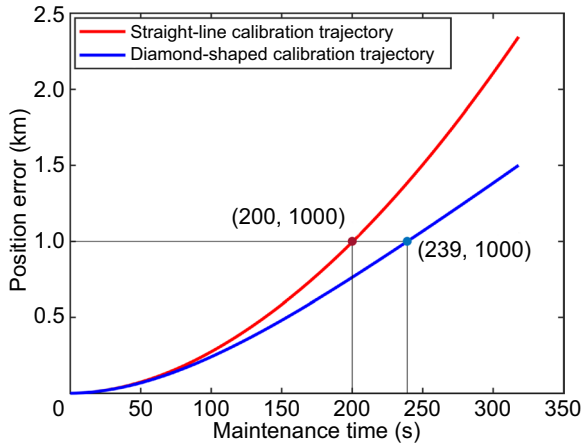

Fig. 15 Maintenance time for SINS position error to diverge by 1 km by different trajectories in the field experiment

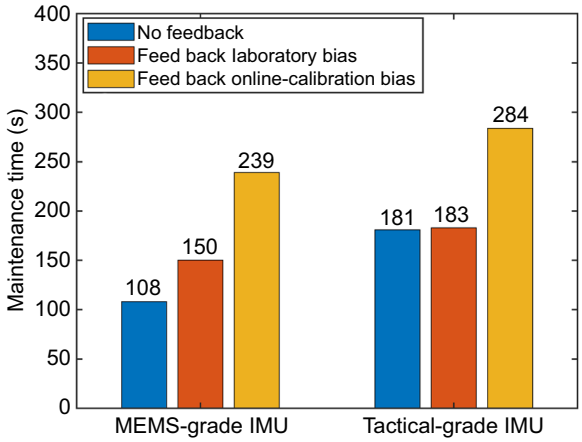

Fig. 16 Comparison of the maintenance time for SINS position error to reach 1 km with different grade IMU and different calibration schemes

38.9%, indicating the effectiveness of the proposed calibration algorithm.

In the future, when a relay reference network is designed and established, we plan to conduct the field experiment to calibrate the different-leveled IMU sensors with the proposed algorithm, thus achieving the goal of long-term and long-distance underwater navigation.

Acknowledgements
The authors are grateful to the experiment team from The First Institute of Oceanography,Ministry of Natural Resources of China, Harbin Engineering University and Wuhan University for collecting the data used in the study.

Author contributions
W.N proposes the idea of IMU calibration by acoustic LBL and revises the manuscript. P.W is responsible for experimental calculation, analysis and writing the draft manuscript. Y.L provides data analysis support. T.X provides program guidance. All authors read and approved the final manuscript.

Funding
This study is sponsored by "Laoshan Laboratory (No. LSKJ202205100, LSKJ202205104), National Natural Science Foundation of China (41931076) and the Young Scholars Program of Shandong University, Weihai.

Availability of data and materials
The datasets used and analyzed in this study are available from the corresponding author on reasonable request.

Declarations

Competing interests
Tianhe Xu is editorial board member for Satellite Navigation and was not involved in the editorial review, or the decision to publish this article. All authors declare that there are no other competing interests.

Received: 27 June 2023 Accepted: 27 November 2023
Published online: 18 March 2024

References

Aggarwal, P., Syed, Z., Niu, X., & El-Sheimy, N. (2008). A standard testing and calibration procedure for low cost MEMS inertial sensors and units. *The Journal of Navigation, 61*(2), 323–336.
Chen, Y., Zheng, D., Miller, P. A., & Farrell, J. A. (2015). Underwater inertial navigation with long baseline transceivers: A near-real-time approach. *IEEE Transactions on Control Systems Technology, 24*(1), 240–251.
Crassidis, J. L. (2006). Sigma-point Kalman filtering for integrated GPS and inertial navigation. *IEEE Transactions on Aerospace and Electronic Systems, 42*(2), 750–756.
Es-sadaoui, R., Guermoud, M., Khallaayoune, J., & Brizard, T. (2018). Autonomious Underwater Vehicles Navigation and Localization Systems: A Survey. *Smart Application and Data Analysis for Smart Cities (SADASC'18)*.
Fujita, M., Ishikawa, T., Mochizuki, M., Sato, M., Toyama, S. I., Katayama, M., & Colombo, O. L. (2006). GPS/Acoustic seafloor geodetic observation: method of data analysis and its application. *Earth, Planets and Space, 58*(3), 265–275.
Goshen-Meskin, D., & Bar-Itzhack, I. Y. (1992). Observability analysis of piecewise constant systems. II. Application to inertial navigation in-flight alignment (military applications). *IEEE Transactions on Aerospace and Electronic Systems, 28*(4), 1068–1075.
Groves, P. D. (2015). Principles of GNSS, inertial, and multisensor integrated navigation systems, [Book review]. *IEEE Aerospace and Electronic Systems Magazine, 30*(2), 26–27.
Han, S., Wang, J., & Knight, N. (2009). Using allan variance to determine the calibration model of inertial sensors for GPS/INS integration. In *6th Interational Symposium on Mobile Mapping Technology*.
Kebkal, K. G., & Mashoshin, A. I. (2017). AUV acoustic positioning methods. *Gyroscopy and Navigation, 8*(1), 80–89.
Lee, W., Eckenhoff, K., Geneva, P., & Huang, G. (2020). Intermittent GPS-aided vio: Online initialization and calibration. In *2020 IEEE International Conference on Robotics and Automation (ICRA)* (pp. 5724–5731). IEEE.
Leonard, J. J., & Bahr, A. (2016). *Autonomous underwater vehicle navigation* (pp. 341–358). Springer handbook of ocean engineering.
Leonard, J.J., Bennett, A.A., Smith, C.M., & Feder, H.J.S. (1998). Autonomous Underwater Vehicle Navigation.
Levin, L. A., Bett, B. J., Gates, A. R., Heimbach, P., Howe, B. M., Janssen, F., & Weller, R. A. (2019). Global observing needs in the deep ocean. *Frontiers in Marine Science, 6*, 241.
Matsumoto, H., & Araki, E. (2021). Drift Characteristics of DONET pressure sensors determined from in-situ and experimental measurements. *Frontiers in Earth Science, 8*, 600966.
Medwin, H., & Clay, C. S. (1998). Fundamentals of acoustical oceanography academic. *New York*, p. *24*.
Meyer, H. J., & Jacob, T. (1994). High accuracy navigation and landing system using GPS/IMU system integration. *IEEE Aerospace and Electronic Systems Magazine, 9*(7), 11–17.
Miller, K. A., Thompson, K. F., Johnston, P., & Santillo, D. (2018). An overview of seabed mining including the current state of development, environmental impacts, and knowledge gaps. *Frontiers in Marine Science, 4*, 418.
Milne, P.H. (1983). Underwater acoustic positioning systems.
Paull, L., Saeedi, S., Seto, M., & Li, H. (2013). AUV navigation and localization: A review. *IEEE Journal of Oceanic Engineering, 39*(1), 131–149.
Paull, L., Seto, M., Saeedi, S., & Leonard, J. J. (2018). Navigation for Underwater Vehicles. In M. H. Ang, O. Khatib, & B. Siciliano (Eds.), *Encyclopedia of Robotics* (pp. 1–15). Springer, Berlin Heidelberg.
Poddar, S., Kumar, V., & Kumar, A. (2017). A comprehensive overview of inertial sensor calibration techniques. *Journal of Dynamic Systems, Measurement, and Control, 139*(1), 011006.
Ru, X., Gu, N., Shang, H., & Zhang, H. (2022). MEMS inertial sensor calibration technology: Current status and future trends. *Micromachines, 13*(6), 879.
Stojanovic, T. A., & Farmer, C. J. (2013). The development of world oceans & coasts and concepts of sustainability. *Marine Policy, 42*, 157–165.
Stutters, L., Liu, H., Tiltman, C., & Brown, D. J. (2008). Navigation technologies for autonomous underwater vehicles. *IEEE Transactions on Systems, Man, and Cybernetics, Part C (applications and Reviews), 38*(4), 581–589.
Titterton, D., & Weston, J. L. (2004). *Strapdown inertial navigation technology* (Vol. 17). IET.
Vickery, K. (1998). Acoustic positioning systems. A practical overview of current systems. In *Proceedings of the 1998 Workshop on Autonomous Underwater Vehicles (Cat. No. 98CH36290)* (pp. 5–17). IEEE.
Wynn, R. B., Huvenne, V. A., Le Bas, T. P., Murton, B. J., Connelly, D. P., Bett, B. J., & Hunt, J. E. (2014). Autonomous Underwater Vehicles (AUVs): Their past, present and future contributions to the advancement of marine geoscience. *Marine Geology, 352*, 451–468.
Yang, Y., Liu, Y., Sun, D., Xu, T., Xue, S., Han, Y., & Zeng, A. (2020). Seafloor geodetic network establishment and key technologies. *Science China Earth Sciences, 63*, 1188–1198.
Yang, Y., Ren, X., Jia, X., & Sun, B. (2023). Development trends of the national secure PNT system based on BDS. *Science China Earth Sciences, 66*, 1–10.
Zhang, J., Han, Y., Zheng, C., & Sun, D. (2016a). Underwater target localization using long baseline positioning system. *Applied Acoustics, 111*, 129–134.
Zhang, T., Shi, H., Chen, L., Li, Y., & Tong, J. (2016b). AUV positioning method based on tightly coupled SINS/LBL for underwater acoustic multipath propagation. *Sensors, 16*(3), 357.
Zhao, S., Wang, Z., He, K., & Ding, N. (2018). Investigation on underwater positioning stochastic model based on sound ray incidence angle. *Acta Geodaetica Et Cartographica Sinica, 47*(9), 1280.

Publisher's Note